Article

Double Gold/Nitrogen Nanosecond-Laser-Doping of Gold-Coated Silicon Wafer Surfaces in Liquid Nitrogen

Sergey Kudryashov [1,*], Alena Nastulyavichus [1,2], Victoria Pryakhina [3], Evgenia Ulturgasheva [2], Michael Kovalev [1,2], Ivan Podlesnykh [1], Nikita Stsepuro [1,2] and Vadim Shakhnov [1]

[1] Department of Design and Manufacturing Technology of Electronic Circuits, Bauman Moscow State Technical University, 105005 Moscow, Russia; nastulyavichusaa@lebedev.ru (A.N.); kovalevms@lebedev.ru (M.K.); i.podlesnykh@lebedev.ru (I.P.); stsepuro.ng@lebedev.ru (N.S.); shakhnov@mail.ru (V.S.)
[2] Lebedev Physical Institute of the Russian Academy of Sciences, 119991 Moscow, Russia; e.ulturgasheva@lebedev.ru
[3] Institute of Natural Sciences and Mathematics, Ural Federal University, 620002 Ekaterinburg, Russia; viktoria.pryahina@urfu.ru
* Correspondence: kudryashovsi@lebedev.ru

Abstract: A novel double-impurity doping process for silicon (Si) surfaces was developed, utilizing nanosecond-laser melting of an 11 nm thick gold (Au) top film and a Si wafer substrate in a laser plasma-activated liquid nitrogen (LN) environment. Scanning electron microscopy revealed a fluence- and exposure-independent surface micro-spike topography, while energy-dispersive X-ray spectroscopy identified minor Au (~0.05 at. %) and major N (~1–2 at. %) dopants localized within a 0.5 µm thick surface layer and the slight surface post-oxidation of the micro-relief (oxygen (O), ~1.5–2.5 at. %). X-ray photoelectron spectroscopy was used to identify the bound surface (SiN_x) and bulk doping chemical states of the introduced nitrogen (~10 at. %) and the metallic (<0.01 at. %) and cluster (<0.1 at. %) forms of the gold dopant, and it was used to evaluate their depth distributions, which were strongly affected by the competition between gold dopants due to their marginal local concentrations and the other more abundant dopants (N, O). In this study, 532 nm Raman microspectroscopy indicated a slight reduction in the crystalline order revealed in the second-order Si phonon band; the tensile stresses or nanoscale dimensions of the resolidified Si nano-crystallites envisioned by the main Si optical–phonon peak; a negligible a-Si abundance; and a low-wavenumber peak of the Si_3N_4 structure. In contrast, Fourier transform infrared (FT-IR) reflectance and transmittance studies exhibited only broad structureless absorption bands in the range of 600–5500 cm^{-1} related to dopant absorption and light trapping in the surface micro-relief. The room-temperature electrical characteristics of the laser double-doped Si layer—a high carrier mobility of 1050 cm^2/Vs and background carrier sheet concentration of ~2×10^{10} cm^{-2} (bulk concentration ~10^{14}–10^{15} cm^{-3})—are superior to previously reported parameters of similar nitrogen-implanted/annealed Si samples. This novel facile double-element laser-doping procedure paves the way to local maskless on-demand introductions of multiple intra-gap intermediate donor and acceptor bands in Si, providing related multi-wavelength IR photoconductivity for optoelectronic applications.

Keywords: nanosecond-laser; Si wafer; top Au film; liquid nitrogen environment; Au/N double-element doping; nano-recrystallization of Si; mid-IR–vis absorption

Citation: Kudryashov, S.; Nastulyavichus, A.; Pryakhina, V.; Ulturgasheva, E.; Kovalev, M.; Podlesnykh, I.; Stsepuro, N.; Shakhnov, V. Double Gold/Nitrogen Nanosecond-Laser-Doping of Gold-Coated Silicon Wafer Surfaces in Liquid Nitrogen. *Technologies* **2024**, *12*, 224. https://doi.org/10.3390/technologies12110224

Academic Editor: Ille C. Gebeshuber

Received: 8 October 2024
Revised: 2 November 2024
Accepted: 4 November 2024
Published: 7 November 2024

Copyright: © 2024 by the authors. Licensee MDPI, Basel, Switzerland. This article is an open access article distributed under the terms and conditions of the Creative Commons Attribution (CC BY) license (https://creativecommons.org/licenses/by/4.0/).

1. Introduction

Currently, silicon (Si) is being revived as a basic nano- and optoelectronic material, being a key component material in CMOS-compatible planar photonic integrated circuits [1], and it is extended in their functionality via heterogeneous integration with III–V heterostructures [2]. Photonic integrated circuits are in great demand in ultrafast

telecommunication and other signal-processing modules, utilizing the ultimate speed of light, ultrafast switching, etc. [3].

The hyperdoping of semiconductors, including Si, through non-equilibrium condensed solid- or liquid-phase mechanisms, such as ion implantation [4,5], pulsed laser melting of surface dopant layers along with the semiconductor substrate [6,7], or doping in pulsed laser-activated chemically active fluids [8–10], is broadly utilized to enhance p-n junction functionality (dimensions, response time, etc.) [11] or specific near-IR or mid-IR light absorption for their optoelectronic response [12,13]. In the latter case, the dopant could form a rather deep intermediate donor (acceptor) impurity band in the semiconductor bandgap [14], still merging with the corresponding conduction (valence) band at high impurity concentrations ~10^{20}–10^{21} cm^{-3} [15], resulting in an "insulator-to-conductor" transition [16]. Additionally, the related spontaneous amorphization of the material is a result of internal impurity-induced stresses [17], along with a considerable reduction in carrier mobility due to their scattering on impurity centers or thermally ionized free carriers [18], and their trapping at the deep impurity-related traps [19], which set a natural doping limit at high doping concentrations, requiring the elaborate management of impurity intra-gap energetic states via the control of dopant concentrations and chemical and charge states [20,21]. Double or even multiple semiconductor doping presents an opportunity to overcome the concentration-related "insulator-to-conductor" transition obstacle via the formation of a few intermediate donor (acceptor) bands across the semiconductor bandgap [22]. So far, double-doping has been performed, as a minimum, in two steps—one for each dopant [23]—with the interference (synergy or competition) of the different dopants during the doping process still being a "black-box" issue, potentially depending on chemicals, concentrations, and other factors.

Recently, a Si wafer was laser-doped by nitrogen (N) in a laser plasma-activated liquid nitrogen (LN) environment [24], similarly to boron carbide in previous studies [10]. Nitrogen impurity is known as a key dopant for improving Si crystalline structures by enhancing oxygen precipitation to improve the intrinsic gettering ability of Si wafers [25], locking dislocations to increase mechanical strength [26], and annihilating microdefects [27] (voids and interstitial-type dislocation aggregates via the accumulation of vacancies in N-V complexes [28]), both in floating-zone-grown and Czochralski-grown Si crystals. Bulk doping with nitrogen atoms in substitutional (N_s) positions as deep donor centers could occur (not only in dislocations, grain boundaries, and cellular structures) when the critical content of nitrogen (~10^{15} atom/cm^3 [29]) is locally exceeded in the Si crystal [30]. By itself, N-doped Si exhibits strong sub-bandgap infrared (IR) absorption [31,32] that is suitable for empowering optoelectronic, photovoltaic, and detector performance [33,34] and offering a wide range of potential applications.

However, the challenging introduction of N into Si via non-equilibrium ion implantation encounters difficulties in producing high N concentrations due to the very low solid and liquid solubility limits of only 4.5×10^{15} and 6.0×10^{18} atoms/cm^3 [35], respectively; crystal damage and amorphization [36]; and the activation of interstitial N into substitutional sites [37], with the dominant and most stable N defect in Si being the di-interstitial pair (N_i-N_i) [38]. Then, additional laser annealing converts nitrogen into active N_s forms, with the highest achieved total N concentration in Si to date being 0.5 ± 0.2 at. % (2.5×10^{20} at./cm^3) [39]. For maximal implanted nitrogen concentrations of below 10^{20} atoms/cm^{-3}, Si remains crystalline, but amorphous Si and SiN appear at nitrogen concentrations above 3×10^{20} atoms/cm^{-3}, transforming into precipitated Si_3N_4 upon annealing at 1000 °C or into a continuous layer of crystalline Si_3N_4 for concentrations above 4×10^{22} atoms/cm^3 [40,41], while excess nitrogen is trapped and blisters during high-temperature annealing. Alternatively, reactive laser or plasma-enhanced chemical vapor deposition (PECVD) in a nitrogen atmosphere, which requires high-energy plasma species to activate nitrogen, followed by the thermal annealing of as-deposited films to enhance their crystalline quality, has been reported to produce a-Si_3N_4 films [42,43]. These films show promise for the fabrication of low-loss waveguides and integrated photonic elements [44]. Additionally, direct laser treatment in low-pressure ammonia [42] and high-pressure ammonia or nitrogen

gases [45] facilitates chemical nitridation (a-Si_3N_4 [42]) or doping (up to 6 at. % [45], compared to 12 at. % achieved via PECVD [31]) of the Si surface, respectively.

In this study, we investigated double-doping of Si (Si) wafers through nanosecond-laser plasma-mediated surface nitridation and nitrogen introduction into an undoped crystalline Si wafer coated with a Au film, which was immersed in liquid nitrogen. The effects of laser fluence and exposure time across various laser treatment regimes were examined. Characterization techniques employed included scanning electron microscopy, energy-dispersive X-ray spectroscopy, X-ray photoelectron spectroscopy, and IR and Raman/photoluminescence spectroscopy.

2. Materials and Methods

A 200 µm thick, double-side polished (100) undoped Si wafer (resistivity > 1 kΩ cm) was coated with an 11 nm Au film in an argon atmosphere using magnetron sputtering (SC7620, Quorum Technologies, Lewes, UK). Subsequently, the wafer was immersed in liquid nitrogen (LN, thickness of 20 mm) within a thermally insulating polystyrene foam container. A linear laser scan was conducted over a 3 mm × 2 mm area to facilitate gold and nitrogen doping. The laser scanning was executed using a two-axis micro-positioning stage at scanning speeds of 10, 25, 40, and 60 µm/s, employing a Nd–YAG laser (SOLAR, second harmonic wavelength—532 nm, full-width at half-maximum pulse duration—10 ns, pulse repetition rate—20 Hz). The radiation was focused onto the surface of the immersed sample through a cylindrical lens with a focal length of 20 cm, resulting in a spot size of 2800 × 140 µm after passing through a 2 cm thick LN layer. This produced textured Si regions at laser exposure settings of N = 280, 110, 70, and 50 pulses per spot (see Figure 1). The pulse energies utilized were 10, 14, and 18 mJ, yielding peak laser fluences (F) of 2.5, 3.5, and 4.5 J/cm^2, respectively, for the Si wafer ablation and LN activation (as discussed below).

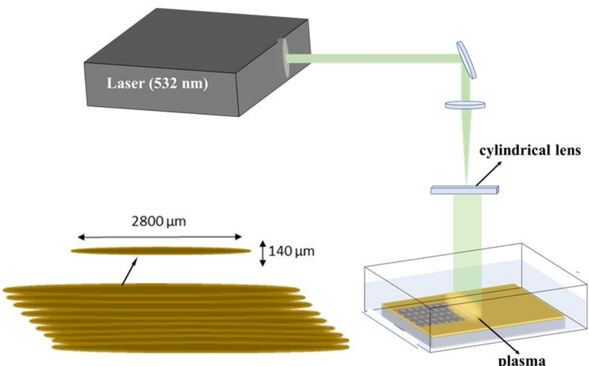

Figure 1. Experimental layout: 532 nm 10-ns Nd–YAG laser, focusing cylindrical lens, thermally-isolating reaction cell with the Si wafer immersed in LN, and 2D micro-positioning stage.

The topographies of the nanopatterned and hyperdoped Si surface were visualized using a VEGA scanning electron microscope (TESCAN, Kohoutovice, Czech Republic), which was equipped with an energy-dispersive X-ray spectrometer (EDX) Explorer 15 for chemical microanalysis at electron beam energies of 3, 5, and 10 keV.

The IR transmittance and reflectance spectra of the nanopatterned and doped Si surface regions, as well as the initial Si wafer, were acquired in ambient air using room-temperature FT-IR spectroscopy (650–2500 cm^{-1}) with a FT-805 spectrometer (SIMEX, Gdańsk, Poland) exhibiting a spectral resolution of 4 cm^{-1}. Top-view structural characterization of the nanopatterned and doped Si surface layers was performed at room temperature via Raman and photoluminescence (PL) microspectroscopy, utilizing a Confotec 520 (SOL Instruments, Augsburg, Germany) microscope–spectrometer at excitation wavelengths of 405 nm and 532 nm, with a spectral resolution of 2 cm^{-1}.

The chemical bonding of Si, nitrogen, oxygen, and carbon atoms was examined across the nanopatterned and doped Si surface layer employing an X-ray photoelec-

tron spectrometer K-Alpha+ (XPS, ThermoFisher Scientific, Waltham, MA, USA, Al Kα, hω = 1486 eV). Photoelectron spectra were acquired using the Al Kα line, achieving an energy accuracy of 0.1 eV and a compositional accuracy of 0.1 atomic percent. The spectrometer was calibrated against the binding energies of Au4f7/2 (83.9 eV), $Ag3d_{5/2}$ (368.2 eV), and $Cu2p_{3/2}$ (932.6 eV). Full-energy-range XPS spectra as well as spectral line regions for Au4f, Si2p, N1s, O1s, and C1s were collected from an analysis area measuring 200 μm in diameter, employing a pass energy of 30 eV and an energy step size of 0.1 eV. A built-in argon ion (Ar+) etching system was utilized for layer-by-layer analysis and the in-depth reconstruction of compositional distribution, using 20 s per etching cycle (10 nm).

3. Results and Discussions

3.1. Surface Topography and Chemical Composition

The interaction of an ns-laser with a Au/Si sample in a LN environment was found to proceed through the formation of an ablative plasma. This interaction resulted in pronounced microscale ablative surface topography and activated nitrogen molecules in the LN via dissociation and electron impact excitation. The experimentally determined ablation threshold fluence was approximately 1 J/cm^2, which was exceeded at peak fluences of 2.5, 3.5, and 4.5 J/cm^2 for all exposure levels ranging from 50 to 280 pulses per spot (see Figure 2). It is well established that at (sub)-GW/cm^2 intensities, nanosecond-laser ablation occurs through a phase explosion that leads to homogeneous boiling of a laser-superheated melt. This process generates a vapor–droplet mixture within a pressurized ablative plume [46]. The higher vapor density and droplet fraction significantly lower the breakdown threshold intensity of the plume, resulting in sub-critical ablative plasma characterized by dissociated or atomized droplets and ionized atoms [46]. The plasma, expanding in the liquid nitrogen on a microsecond timescale, vaporizes, dissociates, and ionizes nitrogen molecules at the contact front between the plume and the LN, creating a bubble filled with low-temperature plasma. During the collapse stage, occurring on a (sub)millisecond timescale, the bubble returns atomic and molecular nitrogen to the Si surface [47], thereby generating high atomic/molecular gaseous nitrogen pressure for doping the material. Furthermore, due to the plasma and the potential screening effects of the bubble on the surface, the influences of fluence and exposure on surface topography are not distinctly observable (see Figure 2).

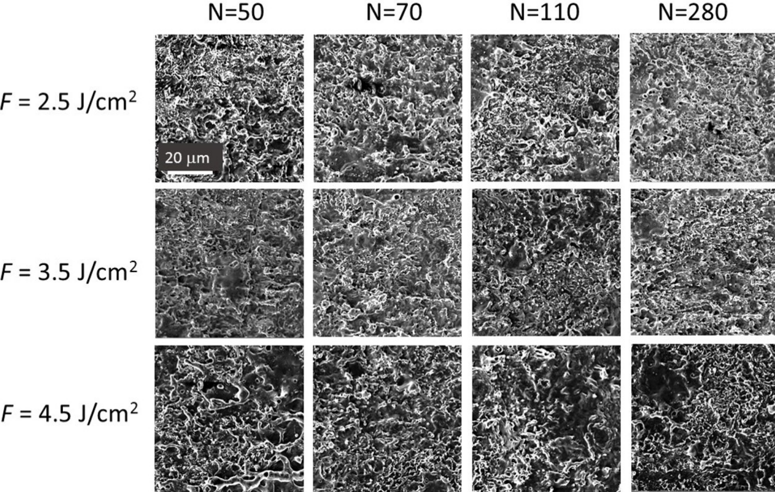

Figure 2. SEM images (15°-degree view) of laser-textured Si wafer topography at different fluences of F = 2.5–4.5 J/cm^2 and exposures of N = 50–280.

Our qualitative EDX mapping indicates the homogeneity of the gold and nitrogen introduction into Si, as demonstrated by the consistent patterns observed in the chemical maps (Figure 3a). Quantitative EDX analysis of the Au and N content in the laser texture was

conducted at energies of 3 keV (with a probe depth in Si of $\delta_3 \approx 0.02$ μm [48]), 5 keV ($\delta_5 \approx 0.15$ μm [46]), and 10 keV ($\delta_{10} \approx 0.65$ μm [48]). The initial Au/Si sample, featuring an 11 nm thick Au film, exhibited relative Au content values of $C_{Au,3} \approx 1.2$ at. % (3 keV), $C_{Au,5} \approx 0.14$ at. % (5 keV), and $C_{Au,10} \approx 0.03 \pm 0.02$ at. % (10 keV) under these acquisition conditions. Following laser treatment, the Au content decreased to $C_{Au/Si,3} \approx$ 0–0.27 at. %, $C_{Au/Si,5} \approx$ 0–0.08 at. %, and $C_{Au/Si,10} \approx (0\text{–}0.04) \pm 0.03$ at. %, contingent upon the laser fluence and exposure (Figure 3b). In addition to laser ablation, it is anticipated that the Au dopant migrates into Si along the thickness of the laser-melted/doped Si layer, with a calculated thickness $d \approx 2\sqrt{\chi\tau} \approx 0.25$ μm for a laser pulse width $\tau \approx 10$ ns and high-temperature thermal diffusivity of Si, $\chi \approx 0.16$ cm^2/s [49]. The corresponding integrated contents can be compared, yielding $C_{Au,3} \times \delta_3 \approx C_{Au,5} \times \delta_5 \approx C_{Au,10} \times \delta_{10} \approx 0.02$ at.%·μm in relation to their values in the laser-produced texture, specifically $C_{Au/Si,3} \times d \leq 0.08$ at.%·μm, $C_{Au/Si,5} \times d \leq 0.02$ at.%·μm, and $C_{Au/Si,10} \times d \leq 0.01 \pm 0.01$ at.%·μm. It is evident that the intermediate EDX analysis regime at 5 kV provides the most reliable estimate of Au content, as shown by $C_{Au,5} \times \delta_5 \approx C_{Au/Si,5} \times d \leq 0.02$ at.%·μm, which is valid for $\delta_5 \leq d$. In contrast, the minimal voltage of 3 kV probes a very thin surface layer of only 20 nm (δ_3 « d), which remains enriched in gold even after laser treatment, as indicated by $C_{Au/Si,3} \times d \leq 0.08$ at.%·μm > $C_{Au,3} \times \delta_3 \approx 0.02$ at.%·μm. Conversely, the layer of thickness 0.6 μm examined via EDX analysis at 10 kV corresponds to scarcely measurable Au concentrations, $C_{Au,10}$, $C_{Au/Si,10} \leq 0.04 \pm 0.03$ at.%. Notably, even at 5 kV, there is considerable variability in the EDX data regarding the relative Au content as a function of laser fluence and exposure, averaging around 0.03–0.04 at. % without any discernible trends (Figure 3b). Thus, it can be concluded that there is minimal laser-ablative removal of gold during the laser treatment.

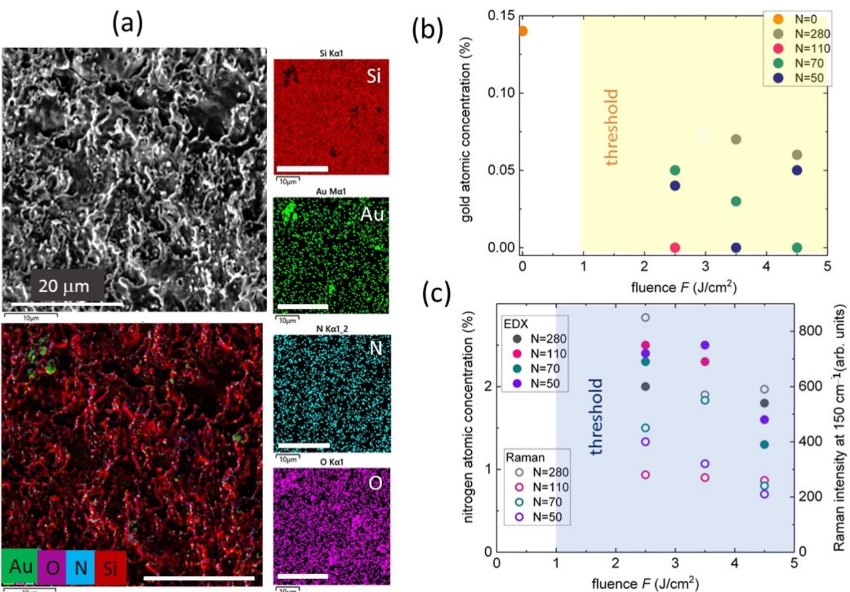

Figure 3. (**a**) Combined and separate EDX elemental maps for gold, oxygen, nitrogen and Si at 5 kV voltage and laser parameters of 3.5-J/cm^2 fluence and 280-pulse exposure. Dependences of gold (**b**) and nitrogen (**c**) atomic content (%) probed at the 5 kV voltage versus laser fluence at different exposures of 50, 70, 110 and 280 pulses/spot. Additionally, the 150 cm^{-1} Raman peak intensity for Si_3N_4 is shown in (**c**) for comparison.

In contrast, N infiltrates Si more readily, achieving significantly higher concentrations (up to 2.5 atomic percent in the 20 nm thick top layer) and penetrating more deeply (the difference in N concentrations at the 5 kV and 10 kV voltages, specifically at depths of 0.15 μm and 0.6 μm, is not substantial, at2.0 ± 0.5 at. % versus 1.5 ± 0.5 at. %, as shown in Figure 3c). However, with respect to nitrogen doping, a distinct trend is observed in this figure; a reduction in N content occurs at higher laser fluences and exposure times, despite a seemingly

stronger activation of the laser plasma when using LN. This reduction may be attributed to enhanced ablative removal of N-doped Si and the ablative shielding of the Si surface from the activated gaseous nitrogen. This trend is consistent with the fluence-dependent decrease in Raman intensity for the 150 cm^{-1} peak associated with β-Si_3N_4 [50] (refer to the subsequent section). Notably, these doping results correlate reasonably well with N contents of 1–3 at. % in 0.3 μm thick Si surface layers that were laser-treated in LN under comparable conditions [24], as well as 1–6 at. % for ns-laser nitridation to depths of approximately 0.6 μm in high-pressure N_2 and NH_3 gases at laser fluences exceeding 2 J/cm^2 [45], and 1–5 at. % in the ~1 μm thick layer during ns-laser induced LN-mediated nitridation of SiC at laser fluences above 2 J/cm^2 [10].

3.2. XPS Depth Profiling of Chemical States for Si and Its Dopants

XPS analysis of the sample surfaces indicates significant oxidation (Si-O, 103.0 eV) and nitridation (Si-N, 101.9 eV) of pure elemental Si, characterized by a doublet of Si2p3/2 at 99.4 eV and Si2p1/2 at 100.0 eV (Figure 4a). The nitrogen signal, N1s, is presented in Figure 4b as part of the SiN_x/Si phase, indicated by a single peak at 397.3 eV [51,52]. Notably, this nitrogen content increases with exposure to nitrogen and decreases with exposure to fluorine (Figure 4f). The presence of the dopant, gold, is represented by the doublet of Au4f5/2 and Au4f7/2, with each line comprising two components: metallic gold (Au_M) and clustered gold (Au_{CL}) [53] (Figure 4c). The overall gold content rises significantly at the maximum fluence of 4.5 J/cm^2 (Figure 4f), likely due to the ablative plasma screening of the sample surface. The typical surface concentrations are approximately 50 at. % for Si, 7–9 at. % for N, approximately 40 at. % for O, and $\leq$0.1 at. % for Au, which are considerably higher owing to the nanometer-scale XPS probing depth, in contrast to the typical energy-dependent (sub)micrometer probing depths observed in EDX.

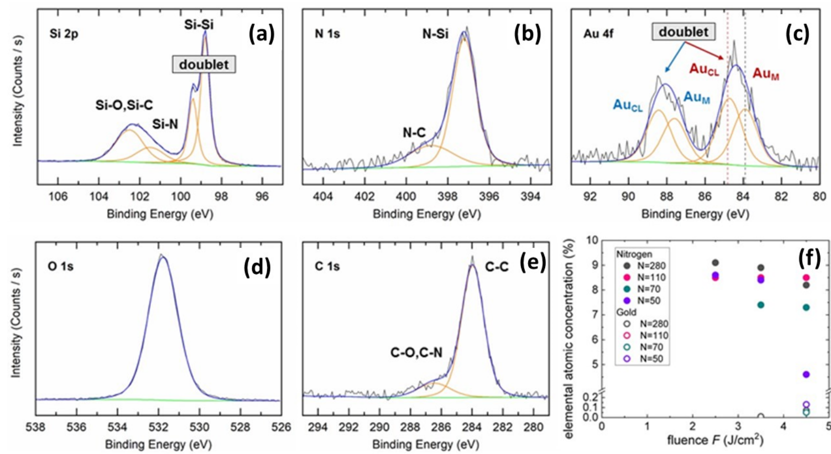

Figure 4. XPS binding energy spectra for Si (**a**), N (**b**), Au (**c**), O (**d**), and C (**e**) elements with their spectral decomposition and assignment after [51]. (**f**) Fluence dependence of elemental atomic content for N (dark symbols) and Au (light symbols) at different laser exposures, N = 50–280 pulses/spot.

During the etching of samples with a 10 nm step in the range of 0–50 nm, a rapid purification of Si in the 10 nm surface layer was observed (Figures 5a and 6a), while the concentrations of other dopants decreased throughout the total 50 nm thick etched layer (Figures 5 and 6). At the minimal fluence of F = 2.5 J/cm^2 (and also at 3.5 J/cm^2), gold is almost absent in the sample (Figure 5d), whereas the concentrations of oxygen and nitrogen components decrease more gradually in the bulk Si (Figure 5b,c). In contrast, at the maximal fluence of F = 2.5 J/cm^2, the emerging gold eventually diminishes in concentration within the bulk Si, with the minor Au_M component decreasing at a faster rate compared to Au_{CL} (Figure 6d). Importantly, within the 50 nm Si layer, the emerging gold displaces nitrogen and oxygen, which remain only at the surface. Surprisingly, even a marginal gold content of approximately 0.1 at. % significantly affects the multi-percent (up to 10 at. %)

concentrations of nitrogen and oxygen, indicating its rapid distribution in the laser melt and preventing the subsequent dissolution of nitrogen and oxygen. The depth-dependent distributions of nitrogen and gold are summarized in Figure 7 below.

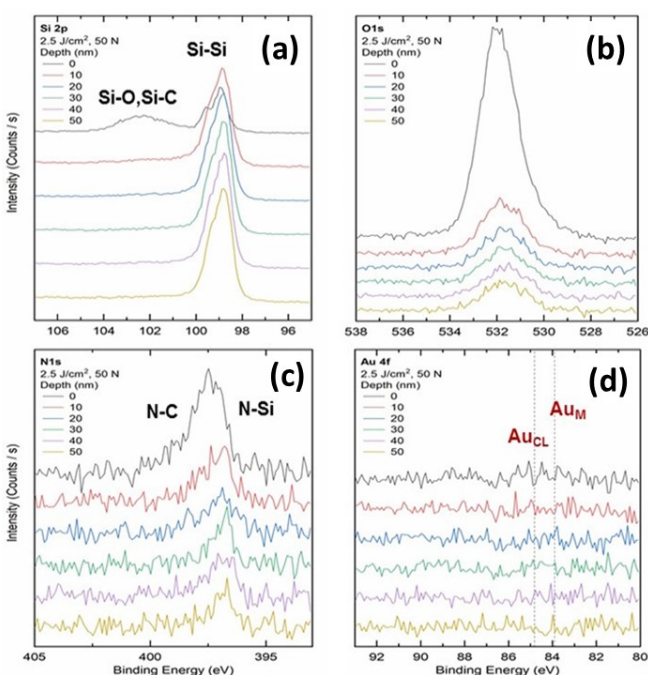

Figure 5. Depth-dependent XPS binding energy spectra for Si (**a**), O (**b**), N (**c**), and Au (**d**) elements with their spectral assignment after [49], acquired at the Si spot modified at F = 2.5 J/cm^2 and N = 50 pulses/spot.

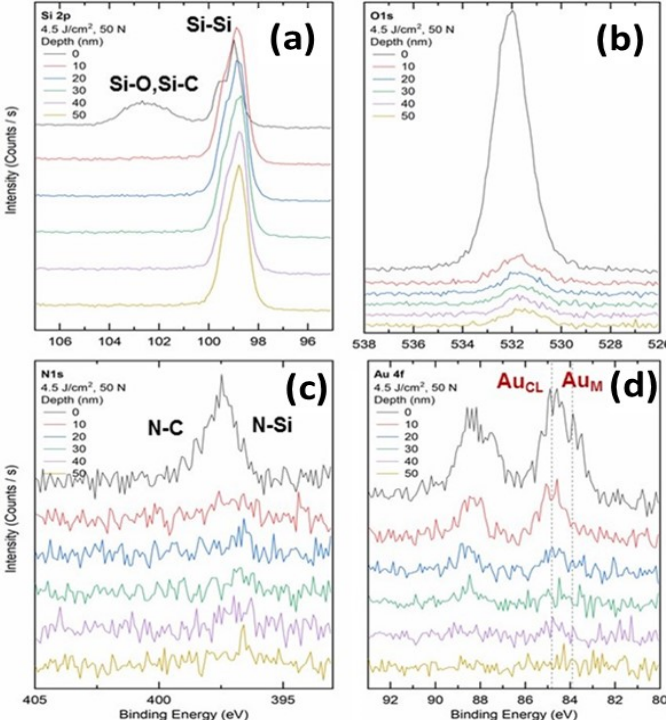

Figure 6. Depth-dependent XPS binding energy spectra for Si (**a**), O (**b**), N (**c**) and Au (**d**) elements with their spectral assignment after [51], acquired at the Si spot modified at F = 4.5 J/cm^2 and N = 50 pulses/spot.

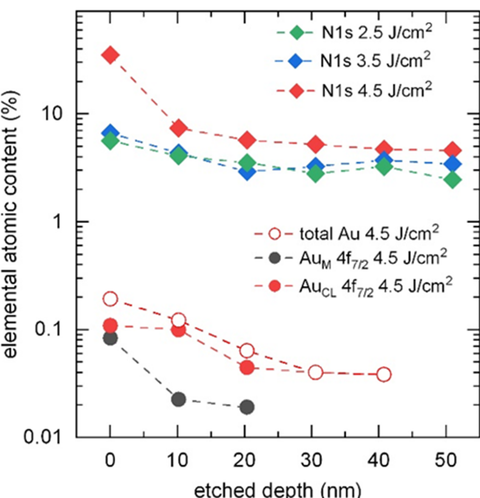

Figure 7. XPS-acquired depth-dependent abundance of nitrogen and gold at laser fluence F = 2.5, 3.5 and 4.5 J/cm^2 for N = 50 pulses/spot. The total gold content acquired for the Au4f$_{7/2}$ line at F = 4.5 J/cm^2 for N = 50 pulses/spot is distinguished between the metallic (Au_M) and cluster (Au_{CL}) components.

3.3. Raman and FT-IR Spectroscopic Characterization

Raman characterization of the laser-modified and doped Si surface layer was conducted using a 532 nm pumping wavelength (Figure 8). The significant penetration depth of 532 nm radiation in crystalline Si (c-Si)—approximately 1 µm [54]—allows for probing the entirety of the modified layer, with the initial c-Si sample serving as a reference. Specifically, the panoramic Raman spectra presented in Figure 8a reveal several characteristic spectral features, such as the prominent LO and TO phonon peak at 521 cm^{-1}, accompanied by a weak shoulder corresponding to a-Si at 480 cm^{-1} (if present); the zone-edge acoustic phonon LA peak at 300 cm^{-1}; and peaks at 144 cm^{-1} and 153 cm^{-1}, which are attributable to β-Si_3N_4 and α-Si_3N_4, respectively [50], within the first-order (one-phonon) Raman region (Raman I). This is further supplemented by a second-order (two-phonon) Raman band observed in the range of 960–970 cm^{-1} (Raman II). Interestingly, in comparison to the reference c-Si spectra, no Raman peaks indicative of doping nitrogen centers [32,55] were detected at Raman wavenumbers exceeding 500 cm^{-1}.

The primary LO and TO Raman peak at 521 cm^{-1} exhibits a slight redshift in both the laser-modified Si and the initial gold/Si samples (Figure 8b) when compared to the reference crystalline Si sample. The observed minor shifts, which are fluence- and exposure-dependent ($\Delta\omega \approx$ 2–4 cm^{-1}), may be attributed to either tensile stresses present in the laser-modified surface layer [56] or to the nanocrystalline nature of the recrystallized material [57,58], characterized by its nanocrystallite size D [57]

$$D = a\left(\frac{A}{\Delta\omega}\right)^{1/\gamma} \tag{1}$$

where the calibration constant A = 47.41 cm^{-1}, the Si lattice parameter a = 0.543 nm, and the exponent γ = 1.44 [57]. The calculated Si nanocrystallites exhibit size variations primarily within the range of D = 4–6 nm, exhibiting an almost independent behavior relative to the laser fluence and exposure duration (Figure 8b, inset). Similarly, the second-order (Raman II) band observed at 960–970 cm^{-1}, which typically reflects the crystalline quality of the Si lattice, shows negligible variation in peak intensity and appears largely unaffected by changes in laser fluence and exposure (Figure 8c). In contrast, the peaks at 144 cm^{-1} corresponding to β-Si_3N_4 and at 153 cm^{-1} associated with α-Si_3N_4 [50]—which are sensitively detected by Raman spectroscopy as indicative of a nitrified Si surface layer—exhibit a distinct trend of reduced intensity as a function of increasing laser fluence (Figure 3c), as previously discussed in the earlier section.

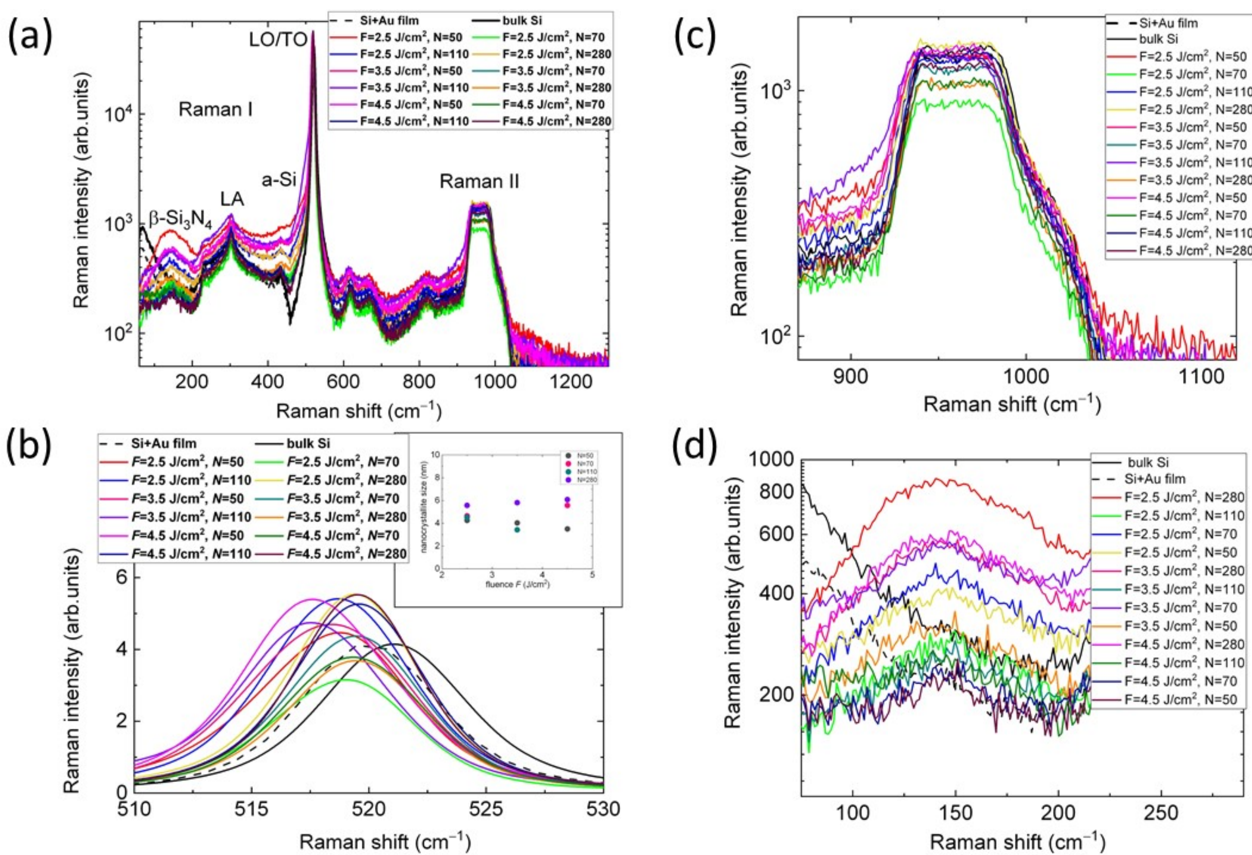

Figure 8. Raman spectra of the laser-doped samples, prepared at different fluence and exposure values, at 532 nm pumping (reference sample—c-Si): (**a**) panoramic view; (**b**) main 521 cm^{-1} LO/TO Raman peak fitted by Lorentzian curves (inset—Si crystallite dimensions derived from the FWHM values of the peak, versus laser fluence); (**c**) second-order Si band; (**d**) low-wavenumber Si_3N_4 band. Spectral assignments after [32,50,55].

In comparison, FT-IR spectroscopy is associated with multi-micrometer penetration depths in IR-transparent Si [54], rendering it relatively insensitive to sub-micrometer-thick surface modifications, such as optically thin surface layers of amorphous Si_3N_4 phases (a-, α-, or β-) with absorption ranges of 700–1100 cm^{-1} [24,50,59]. Specifically, in our study, the microtextured/doped Si surfaces exhibit significant broadband light scattering and trapping within the range of 2–10 μm, which is evidenced by the markedly reduced IR reflectance and transmittance measured in air (Figure 9). The increase in the extinction coefficient at high wavenumbers indicates that the long-wavelength absorption of free carriers, potentially arising from the thermal ionization of predominant donor nitrogen centers and present within gold nanoparticles, is negligible (as further discussed in our electro-physical characterization data below). Thus, the IR absorption characteristics are primarily attributed to the nitrogen pair (N_i-Ni) centers at 770 and 960 cm^{-1} [55], off-center substitutional nitrogen (N_s) at 550, 770, and 890 cm^{-1} [55], and aggregates involving vacancies (V) and Si self-interstitials (I)—(N_s-N_s), (N_i-N_i)V, (N)2I, etc. [32]. These features are further enhanced at lower wavenumbers due to scattering and trapping occurring within the microscale topographical relief. Importantly, the spectral variations in reflectance, transmittance, and extinction coefficient are minimized at the maximum fluence of F = 4.5 J/cm^2, corroborating the observation of stronger ablative plasma screening on the Si surface under this fluence and the associated exposures.

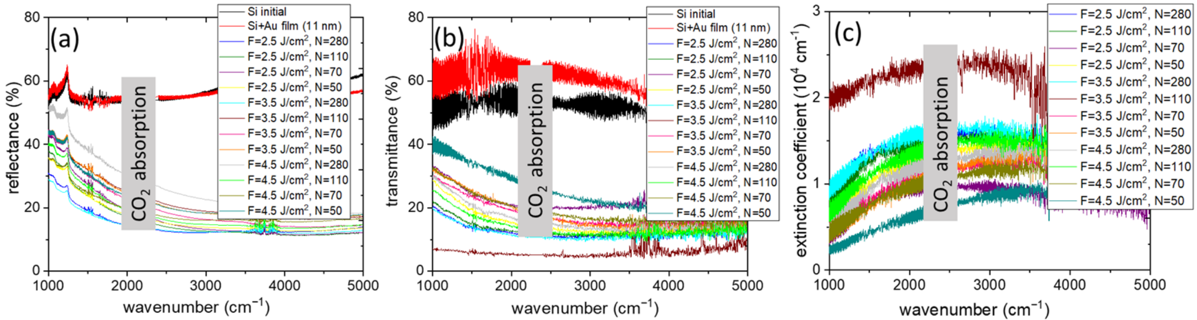

Figure 9. FT-IR reflectance (**a**), transmittance (**b**) and extinction coefficient (**c**) spectra of laser-modified/doped samples prepared at different fluence and exposure values (reference sample—c-Si).

Finally, we conducted room-temperature van der Pauw and Hall measurements to evaluate the electrical characteristics of the laser-modified Si surface layer. The results demonstrate a high carrier mobility of 1050 cm^2/Vs and a carrier sheet concentration of approximately 2×10^{10} cm^{-2} (with a bulk concentration of roughly 10^{14}–10^{15} cm^{-3}), which are reasonably consistent with the corresponding room-temperature parameters observed in nitrogen-implanted and annealed Si samples, reported to be in the range of (3–4) $\times 10^2$ cm^2/Vs and approximately 10^{17} cm^{-3} [40]. The high carrier mobility suggests a favorable crystalline quality of the layer, while the relatively low carrier concentration implies negligible dopant segregation effects and minimal thermal ionization of the deep donor states associated with nitrogen (0.2–0.3 eV [40]) as well as the donor and acceptor states related to gold (Au donor/acceptor centers) in Si. Consequently, the observed tensile stress softening of the Si optical phonon [56] appears to be a result of the laser-doping process rather than the formation of nanometer-scale Si crystallites, which would significantly reduce carrier mobility—a scenario that does not apply in this case. Overall, the enhanced mid-infrared absorbance combined with the favorable electrophysical characteristics of the hyperdoped Si layer indicates its potential as a promising optoelectronic material.

4. Conclusions

A novel double-impurity doping process for Si surfaces was investigated in relation to laser fluence and exposure, employing a nanosecond-laser co-melting technique with a top Au film and a Si wafer substrate within a laser plasma-activated LN environment. Laser fluences of 2.5, 3.5, and 4.5 J/cm^2 were selected, as they exceeded the threshold fluence of approximately 1 J/cm^2 necessary for the formation of ablative plasma on the Si surface in LN. This approach aimed to activate the molecular LN for Si doping; however, it primarily resulted in increased plasma screening of the Si surface at higher fluences. In this context, the effect of exposure demonstrated ambiguous influence on the various characteristics of the laser-modified Si layer.

Specifically, the surface micro-spike topography, which is independent of fluence and exposure, exhibited minor amounts of gold (~0.1 at.%) and major amounts of nitrogen (~10 at.%) dopants, localized within a surface layer less than 100 nm thick. X-ray photoelectron spectroscopy revealed the presence of bound surface (SiN_x) and bulk nitrogen doping states. The bulk distributions of both nitrogen and oxygen dopants were significantly diminished due to the competing effect of gold dopants, which exhibited concentrations that were two orders of magnitude lower. A slight reduction in crystalline order was observed through analysis of the second-order Si phonon band, alongside tensile stresses (rather than nanoscale dimensions of the resolidified Si nanocrystallites), negligible amounts of a-Si, and a Si_3N_4 surface coating layer. FT-IR spectroscopy displayed broad, structureless absorption bands in the range of 1000–5000 cm^{-1}, which were associated with dopant absorption and light trapping within the surface micro-relief. The room-temperature electrical characteristics of the laser-nitrified Si layer—exhibiting a carrier mobility of approximately 1×10^3 cm^2/Vs and a background carrier sheet concentration between 10^{14} and 10^{15} cm^{-3}—suggested an almost defect-free structure of the doped layer, devoid of abundant thermally ionized shallow impurity centers and gold-

segregated nanoparticles. These characteristics were superior when compared to previously reported results for nitrogen-implanted and annealed Si samples. This novel, straightforward double-element laser-doping procedure paves the way for the localized, maskless, on-demand introduction of multiple intra-gap intermediate donor and acceptor bands in Si. This approach offers high mobility and low thermal ionization, resulting in excellent broadband infrared photoconductivity performance, which has significant potential for optoelectronic applications.

Author Contributions: Conceptualization, S.K. and V.S.; methodology, S.K. and M.K.; formal analysis, M.K., A.N. and I.P.; investigation, A.N., N.S. and E.U.; writing—original draft preparation, S.K.; writing—review and editing, V.S.; visualization, E.U. and V.P.; supervision, S.K.; All authors have read and agreed to the published version of the manuscript.

Funding: These results were obtained within the framework of the State task № FSFN-2024-0019.

Institutional Review Board Statement: Not applicable.

Informed Consent Statement: Not applicable.

Data Availability Statement: The additional data are available upon special request.

Conflicts of Interest: The authors declare no conflicts of interest.

References

1. Huang, C.; Fujisawa, S.; de Lima, T.F.; Tait, A.N.; Blow, E.C.; Tian, Y.; Bilodeau, S.; Jha, A.; Yaman, F.; Peng, H.T.; et al. A silicon photonic–electronic neural network for fibre nonlinearity compensation. *Nat. Electron.* **2021**, *4*, 837–844. [CrossRef]
2. Xiang, C.; Jin, W.; Huang, D.; Tran, M.A.; Guo, J.; Wan, Y.; Xie, W.; Kurczveil, G.; Netherton, A.M.; Liang, D.; et al. High-performance silicon photonics using heterogeneous integration. *IEEE J. Sel. Top. Quantum Electron.* **2021**, *28*, 8200515. [CrossRef]
3. Carroll, L.; Lee, J.S.; Scarcella, C.; Gradkowski, K.; Duperron, M.; Lu, H.; Zhao, Y.; Eason, C.; Morrissey, P.; Rensing, M.; et al. Photonic packaging: Transforming silicon photonic integrated circuits into photonic devices. *Appl. Sci.* **2016**, *6*, 426. [CrossRef]
4. Tong, Z.; Bu, M.; Zhang, Y.; Yang, D.; Pi, X. Hyperdoped silicon: Processing, properties, and devices. *J. Semicond.* **2022**, *43*, 093101. [CrossRef]
5. Recht, D.; Smith, M.J.; Charnvanichborikarn, S.; Sullivan, J.T.; Winkler, M.T.; Mathews, J.; Warrender, J.M.; Buonassisi, T.; Williams, J.S.; Gradečak, S.; et al. Supersaturating silicon with transition metals by ion implantation and pulsed laser melting. *J. Appl. Phys.* **2013**, *114*, 124903. [CrossRef]
6. Lim, S.Q.; Williams, J.S. Electrical and Optical Doping of Silicon by Pulsed-Laser Melting. *Micro* **2021**, *2*, 1–22. [CrossRef]
7. Fu, J.; Yang, D.; Yu, X. Hyperdoped crystalline silicon for infrared photodetectors by pulsed laser melting: A review. *Phys. Status Solidi* **2022**, *219*, 2100772. [CrossRef]
8. Kudryashov, S.I.; Nguyen, L.V.; Kirilenko, D.A.; Brunkov, P.N.; Rudenko, A.A.; Busleev, N.I.; Shakhmin, A.L.; Semencha, A.V.; Khmelnitsky, R.A.; Melnik, N.N.; et al. Large-scale laser fabrication of antifouling silicon-surface nanosheet arrays via nanoplasmonic ablative self-organization in liquid CS2 tracked by a sulfur dopant. *ACS Appl. Nano Mater.* **2018**, *1*, 2461–2468. [CrossRef]
9. Kudryashov, S.; Nastulyavichus, A.; Kirilenko, D.; Brunkov, P.; Shakhmin, A.; Rudenko, A.; Melnik, N.; Khmelnitskii, R.; Martovitskii, V.; Uspenskaya, M.; et al. Mid-Ir-sensitive n/p-J.unction fabricated on p-type Si surface via ultrashort pulse laser n-type hyperdoping and high-temperature annealing. *ACS Appl. Electron. Mater.* **2021**, *3*, 769–777. [CrossRef]
10. Shimabayashi, M.; Kaneko, T.; Sasaki, K. Nitriding of 4H-SiC by irradiation of fourth harmonics of Nd: YAG laser pulses in liquid nitrogen. *SN Appl. Sci.* **2020**, *2*, 1167. [CrossRef]
11. Sher, M.-J.; Hemme, E.G. Hyperdoped silicon materials: From basic materials properties to sub-bandgap infrared photodetectors. *Semicond. Sci. Technol.* **2023**, *38*, 033001. [CrossRef]
12. Ferdous, N.; Ertekin, E. Atomic scale origins of sub-band gap optical absorption in goldhyperdoped silicon. *AIP Adv.* **2018**, *8*, 055014. [CrossRef]
13. Kudryashov, S.; Boldyrev, K.; Nastulyavichus, A.; Prikhod'ko, D.; Tarelkin, S.; Kirilenko, D.; Brunkov, P.; Shakhmin, A.; Khamidullin, K.; Krasin, G.; et al. Near-far IR photoconductivity damping in hyperdoped Si at low temperatures. *Opt. Mater. Express* **2021**, *11*, 3792–3800. [CrossRef]
14. Sher, M.-J.; Mazur, E. Intermediate band conduction in femtosecond-laser hyperdoped silicon. *Appl. Phys. Lett.* **2014**, *105*, 032103. [CrossRef]
15. Shao, H.; Liang, C.; Zhu, Z.; Ning, B.Y.; Dong, X.; Ning, X.J.; Zhao, L.; Zhuang, J. Hybrid functional studies on impurity-concentration-controlled band engineering of chalcogen-hyperdoped silicon. *Appl. Phys. Express* **2013**, *6*, 085801. [CrossRef]
16. Ertekin, E.; Winkler, M.T.; Recht, D.; Said, A.J.; Aziz, M.J.; Buonassisi, T.; Grossman, J.C. Insulator-to-metal transition in selenium-hyperdoped silicon: Observation and origin. *Phys. Rev. Lett.* **2012**, *108*, 026401. [CrossRef]
17. Vavilov, V.S.; Chelyadinskii, A.R. Impurity ion implantation into silicon single crystals: Efficiency and radiation damage. *Phys. Uspekhi* **1995**, *38*, 333–343. [CrossRef]

18. Dissanayake, S.S.; Pallat, N.O.; Chow, P.K.; Lim, S.Q.; Liu, Y.; Yue, Q.; Fiutak, R.; Mathews, J.; Williams, J.S.; Warrender, J.M.; et al. Carrier lifetimes in gold–hyperdoped silicon—Influence of dopant incorporation methods and concentration profiles. *APL Mater.* **2022**, *10*, 111106. [CrossRef]
19. Sher, M.J.; Simmons, C.B.; Krich, J.J.; Akey, A.J.; Winkler, M.T.; Recht, D.; Buonassisi, T.; Aziz, M.J.; Lindenberg, A.M. Picosecond carrier recombination dynamics in chalcogen-hyperdoped silicon. *Appl. Phys. Lett.* **2014**, *105*, 053905. [CrossRef]
20. Newman, B.K.; Sher, M.J.; Mazur, E.; Buonassisi, T. Reactivation of sub-bandgap absorption in chalcogen-hyperdoped silicon. *Appl. Phys. Lett.* **2011**, *98*, 251905. [CrossRef]
21. Kudryashov, S.; Nastulyavichus, A.; Krasin, G.; Khamidullin, K.; Boldyrev, K.; Kirilenko, D.; Yachmenev, A.; Ponomarev, D.; Komandin, G.; Lebedev, S.; et al. CMOS-compatible direct laser writing of sulfur-ultrahyperdoped silicon: Breakthrough pre-requisite for UV-THz optoelectronic nano/microintegration. *Opt. Laser Technol.* **2023**, *158*, 108873. [CrossRef]
22. Iori, F.; Degoli, E.; Palummo, M.; Ossicini, S. Novel optoelectronic properties of simultaneously n-and p-doped silicon nanostructures. *Superlattice Microst.* **2008**, *44*, 337–347. [CrossRef]
23. Wang, L.Y.; Zhou, R.H.; Liu, Y.F.; Zheng, C.; Cai, J.F.; He, Y. Simulation and typical application of multi-step diffusion method for MEMS device layers. *Key Eng. Mat.* **2015**, *645*, 341–346. [CrossRef]
24. Kudryashov, S.I.; Nastulyavichus, A.A.; Pryakhina, V.I.; Martovitsky, V.P.; Ulturgasheva, E.V.; Kovalev, M.S.; Podlesnykh, I.; Stsepuro, N.G.; Shakhnov, V.A. Nanosecond-laser nitridation and nitrogen doping of silicon wafer surface in liquid nitrogen. *Ceram. Int.* 2024; *submitted*. [CrossRef]
25. Yang, D.; Ma, X.; Fan, R.; Zhang, J.; Li, L.; Que, D. Oxygen precipitation in nitrogen-doped Czochralski silicon. *Phys. B Condens. Matter.* **1999**, *273*, 308–311. [CrossRef]
26. Akatsuka, M.; Sueoka, K. Pinning effect of punched-out dislocations in carbon-, nitrogen-or boron-doped silicon wafers. *Jpn. J. Appl. Phys.* **2001**, *40*, 1240. [CrossRef]
27. Yang, D.; Chu, J.; Xu, J.; Que, D. Behavior of oxidation-induced stacking faults in annealed Czochralski silicon doped by nitrogen. *J. Appl. Phys.* **2003**, *93*, 8926–8929. [CrossRef]
28. Ammon, W.; Hölzl, R.; Virbulis, J.; Dornberger, E.; Schmolke, R.; Gräf, D. The impact of nitrogen on the defect aggregation in silicon. *J. Cryst. Growth.* **2001**, *226*, 19–30. [CrossRef]
29. Yu, X.; Yang, D.; Hoshikawa, K. Investigation of nitrogen behaviors during Czochralski silicon crystal growth. *J. Cryst. Growth* **2011**, *318*, 178–182. [CrossRef]
30. Masuda, A.; Itoh, K.I.; Matsuda, K.; Yonezawa, Y.; Kumeda, M.; Shimizu, T. Nitrogen-doping effects on electrical, optical, and structural properties in hydrogenated amorphous silicon. *J. Appl. Phys.* **1997**, *81*, 6729–6737. [CrossRef]
31. Sgourou, E.N.; Angeletos, T.; Chroneos, A.; Londos, C.A. Infrared study of defects in nitrogen-doped electron irradiated silicon. *J. Mater. Sci. Mater. Electron.* **2016**, *27*, 2054–2061. [CrossRef]
32. Platonenko, A.; Gentile, F.S.; Pascale, F.; Ferrari, A.M.; D'amore, M.; Dovesi, R. Nitrogen substitutional defects in silicon. A quantum mechanical investigation of the structural, electronic and vibrational properties. *Phys. Chem. Chem. Phys.* **2019**, *21*, 20939–20950. [CrossRef] [PubMed]
33. Wang, W.; Ma, S.X.; Liu, X.; Zhao, Y.; Li, H.; Li, Y.; Ning, X.; Zhao, L.; Zhuang, J. NO_2 gas sensor with excellent performance based on thermally modified nitrogen-hyperdoped silicon. *Sens. Actuators B Chem.* **2022**, *354*, 131193. [CrossRef]
34. Potsidi, M.S.; Kuganathan, N.; Christopoulos, S.-R.G.; Sarlis, N.V.; Chroneos, A.; Londos, C.A. Theoretical investigation of nitrogen-vacancy defects in silicon. *AIP Adv.* **2022**, *12*, 025112. [CrossRef]
35. Yatsurugi, Y.; Akiyama, N.; Endo, Y.; Nozaki, T. Concentration, solubility, and equilibrium distribution coefficient of nitrogen and oxygen in semiconductor silicon. *J. Electrochem. Soc.* **1973**, *120*, 975–979. [CrossRef]
36. Belli, M.; Fanciulli, M. Electron Spin–Lattice Relaxation of Substitutional Nitrogen in Silicon: The Role of Disorder and Motional Effects. *Nanomaterials* **2023**, *14*, 21. [CrossRef]
37. Murakami, K.; Itoh, H.; Takita, K.; Masuda, K. Substitutional nitrogen impurities in pulsed-laser annealed silicon. *Appl. Phys. Lett.* **1984**, *45*, 176–178. [CrossRef]
38. Jones, R.; Hahn, I.; Goss, J.P.; Briddon, P.R.; Oberg, S. Structure and Electronic Properties of Nitrogen Defects in Silicon. *Solid State Phenom.* **2003**, *95–96*, 93–98. [CrossRef]
39. Dong, X.; Li, N.; Zhu, Z. A nitrogen-hyperdoped silicon material formed by femtosecond laser irradiation. *Appl. Phys. Lett.* **2014**, *104*, 091907. [CrossRef]
40. Stein, H.J. Nitrogen in Crystalline Si. *MRS Online Proc. Libr.* **1985**, *59*, 523–535. [CrossRef]
41. Stein, H.J. Nitrogen related donors in silicon. *J. Electrochem. Soc.* **1987**, *134*, 2592. [CrossRef]
42. Kobayashi, S.I. IR spectroscopic study of silicon nitride films grown at a low substrate temperature using very high frequency plasma-enhanced chemical vapor deposition. *World J. Condens. Matter Phys.* **2016**, *6*, 287–293. [CrossRef]
43. Mihailescu, I.N.; Litã, A.; Teodorescu, V.S.; Gyorgy, E.; Alexandrescu, R.; Luches, A.; Martino, M.; Barboricã, A. Synthesis and deposition of silicon nitride films by laser reactive ablation of silicon in low pressure ammonia: A parametric study. *J. Vac. Sci. Technol. A* **1996**, *14*, 1986–1994. [CrossRef]
44. Blumenthal, D.J.; Heideman, R.; Geuzebroek, D.; Leinse, A.; Roeloffzen, C. Silicon nitride in silicon photonics. *Proc. IEEE* **2018**, *106*, 2209–2231. [CrossRef]

45. Barkby, J.; Moro, F.; Perego, M.; Taglietti, F.; Lidorikis, E.; Kalfagiannis, N.; Koutsogeorgis, D.C.; Fanciulli, M. Fabrication of nitrogen-hyperdoped silicon by high-pressure gas immersion excimer laser doping. *Sci. Rep.* **2024**, *14*, 19640. [CrossRef] [PubMed]
46. Ionin, A.A.; Kudryashov, S.I.; Seleznev, L.V. Near-critical phase explosion promoting breakdown plasma ignition during laser ablation of graphite. *Phys. Rev. E—Stat. Nonlinear Soft Matter Phys.* **2010**, *82*, 016404. [CrossRef]
47. Kudryashov, S.I.; Samokhvalov, A.A.; Nastulyavichus, A.A.; Saraeva, I.N.; Mikhailovskii, V.Y.; Ionin, A.A.; Veiko, V.P. Nanosecond-laser generation of nanoparticles in liquids: From ablation through bubble dynamics to nanoparticle yield. *Materials* **2019**, *12*, 562. [CrossRef]
48. Kanaya, K.; Okayama, S. Penetration and energy-loss theory of electrons in solid targets. *J. Phys. D Appl. Phys.* **1972**, *5*, 43. [CrossRef]
49. Kudryashov, S.I.; Allen, S.D. Photoacoustic study of KrF laser heating of Si: Implications for laser particle removal. *J. Appl. Phys.* **2002**, *92*, 5627–5631. [CrossRef]
50. Wada, N.; Solin, S.A.; Wong, J.; Prochazka, S. Raman and IR absorption spectroscopic studies on α, β, and amorphous Si3N4. *J. Non-Cryst. Solids* **1981**, *43*, 7–15. [CrossRef]
51. NIST X-Ray Photoelectron Spectroscopy Database. Available online: https://srdata.nist.gov/xps/ElmComposition (accessed on 15 June 2024).
52. Ermolieff, A.; Bernard, P.; Marthon, S.; Camargo da Costa, J. Nitridation of Si (100) made by radio frequency plasma as studied by in situ angular resolved x-ray photoelectron spectroscopy. *J. Appl. Phys.* **1986**, *60*, 3162–3166. [CrossRef]
53. Peters, S.; Peredkov, S.; Neeb, M.; Eberhardt, W.; Al-Hada, M. Size-dependent XPS spectra of small supported Au-clusters. *Surf. Sci.* **2013**, *608*, 129–134. [CrossRef]
54. Palik, E.D. *Handbook of Optical Constants of Solids*, 3rd ed.; Academic Press: San Diego, CA, USA, 1998; p. 1000.
55. Goss, J.P.; Hahn, I.; Jones, R.; Briddon, P.R.; Öberg, S. Vibrational modes and electronic properties of nitrogen defects in silicon. *Phys. Rev. B* **2003**, *67*, 045206. [CrossRef]
56. Tan, H.S.; Kuok, M.H.; Ng, S.C.; Ong, C.K.; Tang, S.H. Laser-induced lattice tensile strain in silicon. *J. Appl. Phys.* **1984**, *5*, 1116–1118. [CrossRef]
57. Viera, G.; Huet, S.; Boufendi, L. Crystal size and temperature measurements in nanostructured silicon using Raman spectroscopy. *J. Appl. Phys.* **2001**, *90*, 4175–4183. [CrossRef]
58. Ehara, T. Electron spin resonance study of nitrogen-doped microcrystalline silicon and amorphous silicon. *Appl. Surf. Sci.* **1997**, *113*, 126–129. [CrossRef]
59. Luongo, J.P. IR study of amorphous silicon nitride films. *Appl. Spectrosc.* **1984**, *38*, 195–199. [CrossRef]

Disclaimer/Publisher's Note: The statements, opinions and data contained in all publications are solely those of the individual author(s) and contributor(s) and not of MDPI and/or the editor(s). MDPI and/or the editor(s) disclaim responsibility for any injury to people or property resulting from any ideas, methods, instructions or products referred to in the content.